Prototype Design of Satellite Payload for Neutron Spectrum Acquisition

Authors: Xiao-Li Wang, Shu-Cheng Shi, Chen-Yao Han, Yi-Ming Ma, Quan-Qi Shi, Shuai Wang, Jiao Feng, Chen-Yao Han, Quan-Qi Shi

Date: 2025-11-26T00:00:00+00:00

Abstract

In recent years, there have been fewer missions to detect neutrons in low Earth orbits (LEO), and the data obtained have been extremely limited. Studying the distribution of the neutron energy spectrum in LEO satellites through detection can help solve three major scientific problems: the source of particles in the inner radiation belt, information on solar-accelerated particles, and the proportion of neutrons from different sources in near-Earth space. The detection efficiency and accuracy of neutrons are affected by charged and primary particles in the environment and secondary neutrons produced by the spacecraft itself, which has been a hot research topic. The neutron spectrometer developed in this study adopts two combinations of 15 silicon detectors in terms of detector type and arrangement, which are used for neutron detection via the nuclear reaction method and recoil proton method, respectively, in which a 27 μm-thick 6LiF conversion layer is used for thermal neutron detection up to 0.4 eV and a 300 μm-thick high-density polyethylene conversion layer is used for fast neutron detection up to 14 MeV and below. The design of the detector set can also remove the influence of primary charged particles and secondary neutrons in the detection environment to a certain extent, thereby improving the accuracy of neutron detection. In this study, the neutron spectrometer hardware, firmware, software design, and basic performance of the front-end readout chip SKIROC2A were tested. The readout circuit of each channel baseline ADC code was less than 17; thus, the channel consistency was good. The RMS noise of the channel baseline was only 7.1 mV and exhibited good stability. The maximum number of events that could be processed per second is 75. The overall power consumption was 3 W, the weight was 792 g, and the volume was less than 1 dm3 . Furthermore, the neutron spectrometer was tested for principle and detection efficiency using various neutron sources, such as 241Am-Be neutron source, 2.5 MeV neutron beam, and 14 MeV neutron beam, and the experiments were analyzed with corresponding simulations. The experimental data and simulation results were in

good agreement and met the design requirements. The intrinsic detection efficiency of the probes used in the neutron spectrometer was 1.05 % for 14 MeV fast neutrons.

Full Text

Preamble

Prototype Design of a Satellite Payload for Neutron Spectrum Acquisition

Xiao-Li Wang,[1],[2] Shu-Cheng Shi,[1] Chen-Yao Han,[1],† Yi-Ming Ma,[2] Quan-Qi Shi,[1],‡ Shuai Wang,[2] and Jiao Feng[2]

[1]Shandong Key Laboratory of Space Environment and Exploration Technology, School of Space Science and Technology, Institute of Space Sciences, Shandong University, Weihai 264209, China
[2]School of Airspace Science and Engineering, Shandong University, Weihai 264209, China

In recent years, neutron detection missions in low Earth orbit (LEO) have become increasingly rare, yielding extremely limited data. Detecting and studying the distribution of neutron energy spectra in LEO can help address three major scientific questions: the origin of particles in the inner radiation belt, information about solar-accelerated particles, and the relative contributions of neutrons from different sources in near-Earth space. However, neutron detection efficiency and accuracy are affected by charged and primary particles in the environment as well as secondary neutrons produced by the spacecraft itself, making this a critical research challenge.

The neutron spectrometer developed in this study employs two configurations of 15 silicon detectors for neutron detection via the nuclear reaction method and the recoil proton method, respectively. A 27 μm-thick LiF conversion layer is used for thermal neutron detection up to 0.4 eV, while a 300 μm-thick high-density polyethylene (HDPE) conversion layer is used for fast neutron detection up to 14 MeV. The detector design also mitigates the influence of primary charged particles and secondary neutrons in the detection environment, thereby improving neutron detection accuracy. This study presents the hardware, firmware, and software design of the neutron spectrometer, along with performance tests of the front-end readout chip SKIROC2A. The baseline ADC code variation across channels was less than 17, demonstrating good channel-to-channel consistency. The RMS noise of the channel baselines was only 7.1 mV, exhibiting excellent stability. The maximum event processing rate is 75 events per second. The overall power consumption is 3 W, the weight is 792 g, and the volume is less than 1 dm^3. The neutron spectrometer was tested for detection principle and efficiency using various neutron sources, including a ^{2} ^{1}Am-Be neutron source, a 2.5 MeV neutron beam, and a 14 MeV neutron beam, with corresponding simulations performed for analysis. The experimental data and

simulation results showed good agreement and met design requirements. The intrinsic detection efficiency of the probes for 14 MeV fast neutrons was 1.05%.

Keywords: neutron spectrometer, satellite payload, prototype design, Geant4, SKIROC2A

INTRODUCTION

Neutrons in near-Earth space originate from several sources. Galactic cosmic rays can reach Earth' s vicinity and produce neutrons. High-energy solar particle events reaching Earth' s atmosphere trigger secondary neutrons that are detected by ground-based neutron monitors. Secondary neutrons are also produced by interactions between spacecraft materials and solar energetic protons, galactic cosmic rays, and locally trapped protons in radiation belts. Solar neutrons are generated through interactions between solar protons and heavy ions with the Sun' s atmosphere, while lightning neutrons result from interactions between lightning-generated energetic gamma rays and Earth' s atmosphere. Neutron spectrometer measurements in near-Earth space can help solve three major scientific problems: studying the radiation sources of particles in the inner radiation belt, investigating the mechanism of solar neutrons in solar flare particle acceleration, and determining the percentage of neutrons from different sources in near-Earth space through comparison with ground-based lightning observation data.

The current mainstream view holds that cosmic-ray albedo neutron decay is one source of protons in the inner radiation belt, although it was previously thought that electron fluxes at different locations in the radiation belts differed significantly and that other sources might exist. However, data measured from LEO by Li et al. in 2017 showed that albedo neutron decay is a stable source of electrons in radiation belts. Therefore, neutron spectrometer data promise to provide reliable observational evidence to supplement or explain this theory.

Current observations of solar neutron events rely primarily on large neutron detectors constructed in high- and low-latitude areas on the ground. A neutron spectrometer can directly detect solar neutron events outside Earth' s atmosphere, eliminating atmospheric influence and helping detect weaker solar neutron events with clearer signals. It can even observe solar neutron events during periods of relatively infrequent solar activity. Additionally, neutron spectrometers can detect neutrons produced by Earth' s lightning, and in combination with ground-based lightning observation station data, study the contribution of lightning to neutrons in near-Earth space.

The radiation environment in LEO is complex, with several types of high-energy charged primary particles undergoing various nuclear reactions with the neutron detector itself to produce secondary neutrons. Neutron detection must exclude these interference effects, which has led to fewer neutron detection missions for LEO in recent years. In 1989, Keith et al. used various neutron detectors in LEO. For thermal neutrons, they employed a 50 μm Gd shield and other elements

with large neutron capture cross-sections. Fast neutrons were measured using a Bonner ball detector, but the complex structure resulted in a bulky system. In 1991, Dudkin et al. placed several neutron detectors on the Mir space station to measure the neutron energy spectrum in LEO, relying on nuclear 乳胶 and organic scintillator detectors containing Li with a conventional data processing system that could not handle real-time data or large neutron differential flux. In the same year, Korf et al. used organic scintillators to detect neutron differential flux spectra in Earth' s atmosphere, employing plastic scintillator wraps for anti-coincidence. However, the plastic scintillator required gamma-ray shielding, resulting in larger volume and poorer energy resolution. In 2001, Lyagushin et al. used a nuclear 乳胶 detector and nuclear fission foil to detect LEO neutrons inside the Mir space station module, which was more efficient for fast neutrons but sensitive to gamma-ray interference and prone to false triggering. Such detectors typically require fissile materials, resulting in large sizes. In the same year, Matsumoto et al. used a Bonner ball detector to detect neutrons on the ISS, employing a ^{3}He tube detector that was large and fragmented, making it unsuitable for space payload miniaturization. Moreover, the detection efficiency of the ^{3}He tube detector varies with neutron energy, making pre-calibration tedious. The China Space Station has installed an energy particle detector featuring the innovative use of CLYC (Cs LiYCl :Ce) as a neutron measurement sensor, marking the first application of this material in space detection.

Current space neutron detection equipment is generally excessively complex and bulky, resulting in high power consumption that is unsuitable for long-term data acquisition on compact satellites. However, with the development of semiconductor detectors, integrated front-end chips, and high-speed data acquisition and processing systems, it is now possible for space neutron detection payloads to achieve long-term operation, high detection efficiency, and strong anti-jamming capability while ensuring low-power miniaturization.

For neutron detection applications in LEO satellites, our group has constructed a neutron spectrometer based on Si detectors, using LiF and high-density polyethylene (HDPE) as neutron conversion layers for detecting thermal neutrons (< 0.4 eV) and fast neutrons (< 14 MeV). The overall power consumption of the neutron spectrometer is 3 W, which, combined with the power allocation from the satellite, enables continuous operation for one year in orbit. The total weight is 792 g, and the volume is less than 1 dm^{3}. The neutron spectrometer was launched onboard the "Weiming-1" CubeSat in January 2024 into a Sun-synchronous orbit at an altitude of approximately 530 km. On-orbit data from the neutron spectrometer have been accumulated and processed.

II. SYSTEM COMPOSITION

A. Detector Selection

Si detectors offer low density, low leakage current, small size, and high energy resolution, making them widely used for particle detection. Therefore, this study

designed a particle detection system using 15 Si detectors with effective circular area diameters of 35 mm and 28 mm and a thickness of 300 µm. This ensures that particles in the pre-detection energy range produce sufficient deposited energy in the detectors. The package dimensions of the two Si detectors are shown in Fig. 1 [FIGURE:1].

Fig. 1. Detector dimensions: (a) 35 mm, and (b) 28 mm

B. Arrangement of Detectors

For neutron detection in space, the radiation environment is complex, containing both charged particles and neutrons. Therefore, interference from charged particles must be eliminated using the anti-coincidence method. Figure 2 [FIGURE:2] shows a schematic of the anti-coincidence structure, where the upper and lower detectors have larger areas, while the middle detector has a smaller area. Blue represents the conversion layer. Anti-coincidence means that if there is a signal in detectors A or C at the same moment, the signal in detector B at that moment is removed.

Fig. 2. (Color online) Schematic of anti-coincidence structure

The neutron spectrometer detects thermal and fast neutrons with energies up to 14 MeV. To improve detection efficiency and remove the influence of charged particles, the thermal neutron section uses six detectors with Gd shielding in an anti-coincidence detector set. The fast neutron section uses nine detectors, one of which is shared between fast and thermal neutron detection. The arrangement of the neutron spectrometer detectors is illustrated in Fig. 3 [FIGURE:3], comprising 15 silicon semiconductor detectors.

Fig. 3. (Color online) Neutron spectrometer 15-chip detector set

The system includes 15 silicon semiconductor detectors with a thickness of 300 µm. Detector No. 6 is covered with a 300 µm-thick HDPE conversion layer. Detectors No. 11 and 14 are covered with a 27 µm-thick LiF conversion layer. Detectors No. 3, 4, 5, 7, 8, 9, 11, and 14 have an effective circular area with a diameter of 28 mm. Detectors No. 1, 2, 6, 10, 12, 13, and 15 have an effective circular area with a diameter of 35 mm.

Detector No. 1 is used to identify the direction of incoming probe particles. Detectors No. 2–10 are fast neutron detectors, among which No. 3, 4, 5 and No. 7, 8, 9 have the same thickness and effective area. The only difference is that there is a 300 µm-thick HDPE fast-neutron converter layer in front of No. 7, 8, and 9. Detectors No. 3, 4, and 5 can detect signals generated by galactic cosmic rays or other secondary neutrons, whereas recoil proton detectors No. 7, 8, and 9 can also detect recoil proton signals generated by orbital neutrons passing through the HDPE conversion layer. Therefore, under anti-coincidence conditions, the recoil proton spectrum can be obtained by subtracting the total energy spectra of detectors No. 7, 8, and 9 from those of silicon detectors No. 3, 4, and 5. This effectively reduces the influence of background signals on measurements and

improves the accuracy of neutron energy spectrum inversion. The three-layer recoil proton detector has a total thickness of approximately 900 μm, allowing complete deposition of protons up to 14 MeV, even considering oblique incidence. Fast neutrons are detected using the recoil proton method, and the fast neutron energy spectrum is obtained using the least-squares method as a neutron inversion algorithm. Simulation results using Geant4 are shown in Fig. 4 [FIGURE:4].

Fig. 4. Detector thickness required for the full deposition of fast neutrons below 14 MeV at vertical incidence

Detectors No. 10–15 are thermal neutron detectors. Detectors No. 10, 12, 13, and 15, which have larger areas, serve as anti-coincidence detectors, removing charged-particle signals across a wide range of solid angles. A 3 mm-thick Gd sheet is placed between detectors No. 12 and 13 to absorb thermal neutrons, allowing detector No. 11 with the LiF coating to record signal counts generated by reactions of neutrons across all energies with LiF. Detector No. 14 with LiF coating primarily records counts of signals generated by reactions of neutrons other than thermal neutrons with LiF. The thermal neutron flux in orbit can be obtained by dividing the difference in counts between the two detectors by the detection efficiency. Additionally, to distinguish the source direction of thermal neutrons in LEO to some extent, 3 mm-thick Gd is placed around the detector array on all faces except the open side to block thermal neutrons from other directions. The specific position of Gd is shown in Fig. 5

.

Fig. 5. (Color online) Gd placed on five faces around the detector

The blue part represents the 3 mm-thick Gd placed on the five faces around the detector combination. Since the capture cross-sections of thermal neutrons differ for different Gd isotopes and the reaction cross-sections of neutrons with Li vary with energy, the effect of Gd on thermal neutron detection at different energies was analyzed. Si detectors with LiF coatings, both blocked and unblocked by Gd, were simulated using Geant4 to study the variation in detector detection efficiency for thermal neutrons with thermal neutron energy in both cases, as shown in Fig. 6 [FIGURE:6].

Fig. 6. (Color online) Effect of Gd on thermal neutron detection at different energies

The orange data points show the detection efficiency of detector No. 11 for different neutron energies as a function of neutron energy, the blue data points show the detection efficiency of detector No. 14 for different neutron energies as a function of neutron energy, and the gray lines show the reaction cross-sections of Li(n,T) He as a function of neutron energy. The other lines represent the reaction cross-sections of neutrons captured by various Gd isotopes as a function of neutron energy. For thermal neutrons with energies lower than 0.4 eV, the 3 mm-thick Gd can completely block them. The blocking effect of Gd on neutrons

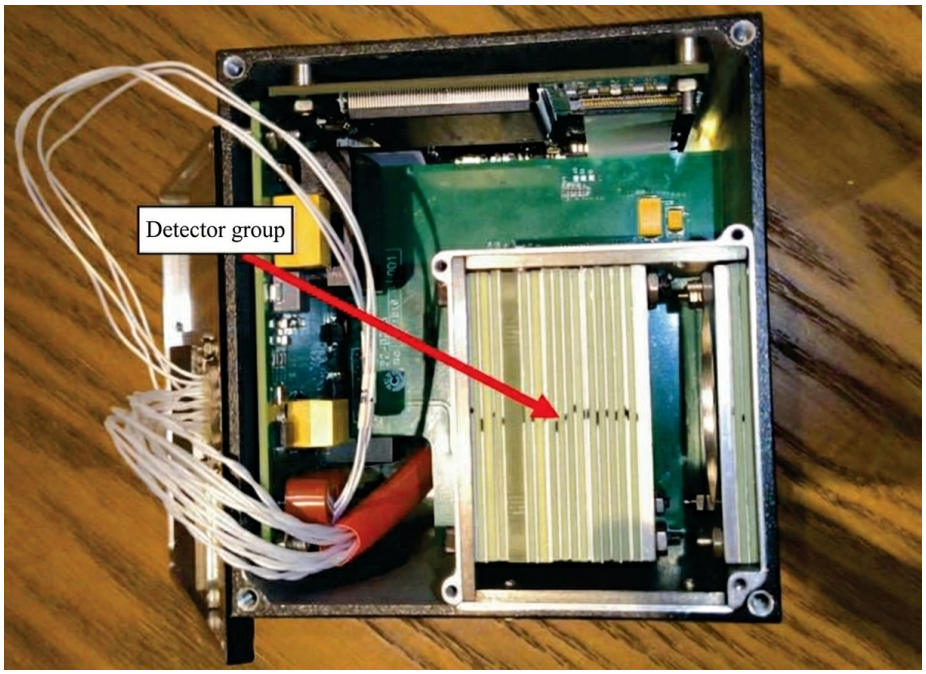

Figure 1: Figure 5

of different energies was considered as a function of detection efficiency in subsequent calculations of orbital thermal neutron flux using neutron spectrometer data.

III. SYSTEM DESIGN

A. Hardware Design

A physical view of the neutron spectrometer is shown in Fig. 7 [FIGURE:7]. An overall hardware block diagram is shown in Fig. 8 [FIGURE:8].

Fig. 7. (Color online) Physical view of neutron spectrometer
Fig. 8. (Color online) Block diagram of neutron spectrometer hardware

Detector signals are directly transmitted to SKIROC2A, which converts the analog signals to digital signals and passes them to the FPGA for data processing. Finally, the FPGA passes the processed data to the MCU. Simultaneously, signals in SKIROC2A are directly connected to the MCU. The MCU is equipped with a CAN interface chip, an Ethernet interface, a USB interface, a UART interface, and SD NAND. The CAN and Ethernet interfaces are used to communicate with the satellite host—CAN transmits commands and telemetry signals, while the Ethernet interface transmits scientific data.

The hardware design consists of three circuit boards: a power supply board, front-end board, and data board. The power-supply board is designed as a low-noise power-supply module that supplies power to all parts of the neutron spectrometer and generates the high-bias voltage required for detector operation. The front-end board is connected to the detector, with the SKIROC2A chip serving as the core of the front-end readout system. SKIROC2A is a 64-channel front-end ASIC designed to read signals from silicon detectors. The data board contains FPGA, MCU, and memory chips.

B. Firmware Design

The firmware design is implemented using a Cyclone series FPGA from Altera. The main purpose is to control SKIROC2A and packetize the data. Since the data format of SKIROC2A cannot be changed and the neutron spectrometer uses only 15 of the 64 channels, considerable invalid information exists in the data packet. To reduce bandwidth and storage pressure, the FPGA must sort valid information from the SKIROC2A memory map and organize it into data packets, which are ultimately passed to the MCU' s file management system for storage. The FPGA firmware consists of several modules: a clock module, trigger module, timing control module, data acquisition module, and SPI module. A block diagram of the primary modules is presented in Fig. 9 [FIGURE:9].

Fig. 9. (Color online) Block diagram of the firmware design module

The clock module generates clock frequencies of 40 MHz and 5 MHz, with 2.5 MHz used in testing. The trigger module is used for test calibration. When SKIROC2A generates a trigger signal, the trigger module controls the external ADC to perform A/D conversion of the charge stored in SKIROC2A. As an external ADC is not used during normal operation, this module remains idle. The timing control module receives and saves the slow control signal for MCU conversion. Before starting acquisition, the module sends the stored slow-control commands to SKIROC2A and controls the timing of single-ended signals. The data acquisition module temporarily stores the SKIROC2A memory map, extracts valid data, and organizes them into packets. The SPI module handles communication between the FPGA and MCU.

C. Software Design

The software design for the neutron spectrometer is realized using an STM32 series MCU with FreeRTOS. A block diagram of the software design is shown in Fig. 10 [FIGURE:10].

Fig. 10. (Color online) MCU combined with FreeRTOS software design of the four main threads

The software design contains four main task threads: FPGA communication processing, interface communication, memory system, and instruction analysis with telemetry generation. In addition to these, the MCU program includes

basic programs such as watchdog and clock subroutines. The FPGA communication processing thread communicates with the FPGA, including SPI initialization, slow control command generation, data processing, and data saving. The interface communication thread controls interfaces with external devices, including USB and UART for ground testing, two CAN interfaces for satellite connection, and Ethernet for direct digital transmission with the satellite. The storage system interface drives the SD NAND flash memory inside the neutron spectrometer and provides file system services using FAT32. The command analysis and telemetry generation thread analyzes commands from CAN and controls other threads. The Star Control Center computer sends fast- and slow-change telemetry polling control sequences over the CAN bus to determine the operating status of the neutron spectrometer.

IV. SYSTEM TESTING AND ANALYSIS

A. Basic Performance Test

After completing the hardware, firmware, and software designs, it is necessary to verify whether the basic performance meets design requirements, including baseline noise RMS, stability, and channel consistency. In this study, the front-end board is connected to the detector, with SKIROC2A as the core of the front-end readout system. Therefore, it is essential to ensure the baseline RMS noise, stability of the 64 SKIROC2A channels, and consistency between channels, as these significantly affect measurement of the deposition energy spectrum.

In the baseline test, the threshold value was set to 255. When the threshold value was close to the baseline reading of the ADC, the trigger circuit continuously generated trigger signals, acquiring and recording the baseline signal of the 64 channels and converting it to numerical values through the internal ADC. The baseline signals of the 64 channels were then Gaussian-fitted, and the ADC value at the peak was taken as the effective channel baseline value. The ADC values of the 64 channel baselines are shown in Fig. 11 [FIGURE:11], where the horizontal axis represents the channel number Nc and the vertical axis represents the ADC readings of the effective baseline value over time.

Fig. 11. ADC value of 64 channel baselines

The baselines of most channels were concentrated between 250 and 265, with baseline differences between different channels less than 17 ADC values, demonstrating good channel-to-channel consistency. As SKIROC2A is a 12-bit ADC with a voltage range of 0.9 V to 2.6 V, the RMS noise of the baseline of all channels was approximately 7.1 mV, showing good stability. In summary, the baseline RMS noise, stability, and channel consistency met the requirements for subsequent experiments.

The average ionization energy of the silicon semiconductor detector used in the neutron spectrometer is 3.6 eV, meaning one electron is ionized per 3.6 eV of deposited energy. Based on the relationship between baseline RMS noise and de-

position energy in the silicon semiconductor detector, the minimum measurable deposition energy of the neutron spectrometer could be determined. The maximum measurable deposition energy was obtained by continuously increasing the input signal through a signal generator until ADC saturation. The electronic system can handle an energy range from 500 keV to 20 MeV, with a maximum event rate of 75 events per second, satisfying the requirements for subsequent experiments.

Additionally, the anti-irradiation performance of the neutron spectrometer was tested as part of the basic performance evaluation. Military-grade components were selected for the hardware, and the software operating system was configured to ensure data validity. In addition to processing memory bad blocks, the neutron spectrometer electronics system is guaranteed to operate continuously for extended periods in high-irradiation environments.

After completing the basic performance test, four major tests were performed: thermal neutron principle test, fast neutron detection principle test, fast neutron detection efficiency test, and coincidence effect test.

B. Thermal Neutron Detection Test

To test the thermal neutron section of the neutron spectrometer in principle, this study used the $^{2\ 1}$Am-Be neutron source from the Institutional Center for Shared Technologies and Facilities (INEST) of the Hefei Institutes of Physical Science, Chinese Academy of Sciences, to test the Si detector containing the LiF coating. The energy spectrum of the $^{2\ 1}$Am-Be neutron source is shown in Fig. 12 [FIGURE:12], with energies ranging from 0 MeV to 11 MeV. The primary fast neutrons produced by the neutron source were slowed by objects such as walls and experimental platforms at the test site, reducing their energy and converting some fast neutrons into lower-energy thermal neutrons.

Fig. 12. $^{2\ 1}$Am-Be neutron source energy spectrum

A Si detector with LiF coating was used in the test. The sensitive layer thickness of the Si detector was 300 µm, with a sensitive area of a 28 mm diameter circle. The LiF coating thickness was approximately 27 µm. The preamplifier used was mesytec-MPR-16L, and the multichannel analyzer was labZY-nanoMCA. The detector was placed in a 2 mm-thick aluminum alloy shielding shell, with a copper mesh outside the shielding shell for electromagnetic interference shielding. The radioactive source and detector were positioned at equal heights. The experimental site layout is illustrated in Fig. 13 [FIGURE:13].

Fig. 13. (Color online) Experimental environment of the $^{2\ 1}$Am-Be neutron source

The red dots represent $^{2\ 1}$Am-Be neutron sources. The $^{2\ 1}$Am-Be neutron source emitted neutrons at a steradian angle of with a flux of approximately 9×10 s ^{1}. The blue part of the back-end experimental platform, wrapped in yellow copper mesh, is the neutron spectrometer. The multichannel spectra obtained

from the experiments were energy-scaled to compare experimental data with simulation results. The truncation position was at approximately 2.7 MeV in the deposition spectrum, and the starting position of the "platform" was at approximately 1 MeV. The energy spectra from approximately 1 MeV to 2.7 MeV were used for "platform" integration, which normalized the experimental data to the simulated energy spectrum, as shown in Fig. 14 [FIGURE:14].

Fig. 14. (Color online) Testing of LiF-coated Si detectors with thermal neutrons after slowing using the $^{2\ 1}$Am-Be neutron source

The blue data points show the multichannel spectral data obtained using the LiF-coated Si detector with the detector positioned approximately 50 cm from the radioactive source. The red data points show multichannel spectral data obtained after placing a 35 mm diameter, 3 mm-thick Gd piece tightly affixed to both sides of the Si detector. The gray line shows the detection effect of the LiF-coated Si detector on thermal neutrons from the $^{2\ 1}$Am-Be neutron source slowed by 5 cm of polyethylene, simulated using Geant4. Since the slowing effect of neutrons by walls and other objects in the experimental environment cannot be easily reproduced in simulation, 5 cm-thick polyethylene was used as a neutron-slowing body placed in front of the detector in the simulation.

In the low-energy region below 1 MeV shown in Fig. 14, some differences exist between the blue data points and the simulated energy spectrum. The experimentally measured low-energy deposited particle signal is greater than in the simulation, caused by electrons produced by $^{2\ 1}$Am-Be neutrons interacting with Gd. The signals considered in the high-energy part of the experiment were not caused by low-energy thermal neutrons but by $^{2\ 1}$Am-Be high-energy fast neutrons that directly reacted with Si nuclei in the detector. Three reasons account for the inconsistency between experimental and simulated data. First, the energy spectrum of the $^{2\ 1}$Am-Be neutron source input to the simulation was a standard spectrum, different from the actual spectrum. Second, the slowing effect on neutrons by walls and other objects in the experimental environment could not be easily reproduced in simulation, so 5 cm-thick polyethylene was used as a neutron-slowing body in the simulation. Finally, noise signals from detector test noise baseline wobbling were not considered in the simulation.

C. Principle Tests of Fast Neutron Detection

To perform principle tests of the fast neutron section, we tested Si detectors containing an HDPE conversion layer using 2.5 MeV and 14 MeV neutron beams and a $^{2\ 1}$Am-Be neutron source from INEST.

1. Testing with 14 MeV Monoenergetic Neutron Beams The 14 MeV monoenergetic neutron beam at INEST utilizes the deuterium-tritium reaction T(D,N) He, generating neutrons emitted outward with a stereo angular distribution of approximately 4 centered on the tritium target point. A Si detector with a sensitive area diameter of 28 mm and thickness of 300 µm was used

in combination with 300 µm-thick HDPE for testing. The preamplifier was mesytec-MPR-16L, and the multichannel analyzer was labZY-nanoMCA. The experimental site plan and Si detector placement are shown in Fig. 15 [FIGURE:15].

Fig. 15. (Color online) 14 MeV neutron beam test site

The Si detector position was approximately on a horizontal plane with the target, about 1.56 m apart. Two control experiments were performed, and the measured multichannel spectral data are shown in Fig. 16 [FIGURE:16].

Fig. 16. (Color online) Data from two control experiments of 14 MeV neutron beam flow

The black line shows the multichannel spectrum generated by 14 MeV neutrons directly bombarding the Si detector, the red line shows the spectrum generated by 14 MeV neutrons bombarding the Si detector covered with a 300 µm-thick HDPE conversion layer, and the blue line shows the difference between the two, with the black and red lines normalized by the peaks near the last 15,500 channels.

To analyze the experimental data, the total deposition energy spectrum produced by a 14 MeV neutron beam on the Si detector and the effect of the HDPE conversion layer on the total deposition energy spectrum were simulated using Geant4, as shown in Fig. 17 [FIGURE:17].

Fig. 17. (Color online) Experimental data of 14 MeV neutron beam simulation using Geant4

The black line shows the multichannel spectrum produced by 14 MeV neutrons in the Si detector, the red line shows the spectrum produced by 14 MeV neutrons bombarding the Si detector covered with a 300 µm-thick HDPE conversion layer, and the blue line shows the difference between the two, where recoil proton signals produced by the reaction between neutrons and hydrogen in the HDPE conversion layer can be observed. The black line in Fig. 16 shows the measured multichannel spectrum, while the black line in Fig. 17 shows the simulated energy spectrum. The difference arises because the simulation did not consider walls and other objects in the environment, energy discrimination problems in the detector, and noise signals generated by detector test noise baseline wobbling during actual testing.

Based on the number of channels at the apex of the descending left edge of the recoil proton multichannel spectrum in the experimental data shown in Fig. 16 and the corresponding energy values at those positions in the recoil proton energy spectrum of Fig. 17, the experimentally measured recoil proton energy spectrum was obtained, as shown in Fig. 18 [FIGURE:18].

Fig. 18. (Color online) Deposition energy spectrum of recoil protons in a 300 µm-thick Si detector

The black data points represent measured data, while the blue lines represent Geant4 simulation results. The experimental data and simulation results show good agreement. As the detector resolution was not included in the simulation, the signal peaks of some reactions are narrower than in the experimental results.

2. ^{241}Am-Be Neutron Source Test The experimental setup is illustrated in Fig. 13. This study used a Si detector with a sensitive region diameter of 35 mm and sensitive layer thickness of 300 µm in combination with a 300 µm-thick HDPE conversion layer for testing. The preamplifier was mesytec-MPR-16L, and the multichannel analyzer was labZY-nanoMCA. The multichannel spectrum of the Si detector was recorded after the measurement period, as shown in Fig. 19 [FIGURE:19].

Fig. 19. (Color online) Testing the fast neutron detection section using the ^{241}Am-Be neutron source

The black line shows the deposition spectrum of ^{241}Am-Be neutrons in the Si detector shielded by two 3 mm-thick Gd plates, the red line shows the deposition spectrum of ^{241}Am-Be neutrons in the Si detector covered by a 300 µm-thick HDPE conversion layer, and the blue line represents the difference between the two. The black and red lines were normalized to the energy spectrum integral from 0.5 MeV to 1 MeV.

The total deposition energy spectrum produced by ^{241}Am-Be neutrons on the Si detector and the effect of the HDPE conversion layer on the total deposition energy spectrum, simulated using Geant4, are shown in Fig. 20 [FIGURE:20].

Fig. 20. (Color online) Total deposited energy spectrum of the ^{241}Am-Be neutron source on the Si detector and the influence of the HDPE conversion layer on the total deposited energy spectrum

The black line represents the deposition spectrum of ^{241}Am-Be neutrons in the Si detector, the red line represents the deposition spectrum of ^{241}Am-Be neutrons bombarding the Si detector covered with a 300 µm-thick HDPE conversion layer, and the blue line represents the difference between the two. The recoil proton signal is produced by the reaction of neutrons and hydrogen in the HDPE conversion layer. The measured recoil proton spectra are compared with simulation results in Fig. 21 [FIGURE:21].

Fig. 21. (Color online) ^{241}Am-Be neutron source bombarding a 300 µm-thick HDPE conversion layer, resulting in a back-scattered proton deposition spectrum in a 300 µm-thick Si detector

The black data points represent measured data, while the blue line represents Geant4 simulation results. The experimental and simulated energy spectra between 1.5 MeV and 7 MeV show good agreement. The poor agreement in the low-energy region is speculated to result from background noise such as gamma rays in the experiment, leading to poor normalization of data from the two experiments.

D. Fast Neutron Detection Efficiency Tests

To test the detection efficiency of the neutron spectrometer for fast neutrons, we used 2.5 MeV and 14 MeV neutron beams from INEST to test a 300 µm-thick Si detector containing a 300 µm-thick HDPE conversion layer. The preamplifier was mesytec-MPR-16L, and the multichannel analyzer was labZY-nanoMCA.

This study used the data shown in Figs. 16 and 18 to calculate the neutron spectrometer detection efficiency for 14 MeV fast neutrons. The total flux of the neutron source at the target is known. The neutron flux hitting the Si detector was calculated based on the detector area and distance from the target. The signal produced by recoil protons from the reaction of fast neutrons with hydrogen nuclei in the detector conversion layer was measured, and the number of fast neutrons detected was counted. In the experiment, the Si detector and target were approximately on the same horizontal plane, with a linear distance of approximately 1.56 m. The detector was irradiated with a 14 MeV neutron beam with a flux of 2.3×10^{1} s^{1}. HDPE was placed in front of the detector and irradiated for 20 min to obtain the multichannel spectrum indicated by the black line in Fig. 15. The intrinsic detection efficiency of the detector for 14 MeV fast neutrons was 1.05%. Detection efficiency is defined as the ratio of the number of signals exceeding the threshold in the detector to the number of neutrons arriving at the detector. The number of neutrons reaching the detector was obtained from the neutron beam flux and the detector distance from the beam target, considering isotropic neutron generation.

Correspondingly, we also compared simulated detection efficiencies at different energy cutoff thresholds, as indicated by the brown line in Fig. 22 [FIGURE:22]. The black data points represent detection efficiencies measured based on experimental data, and the experimental data and simulation results show good agreement.

Fig. 22. (Color online) Detection efficiency of a 300 µm Si detector covered with a 300 µm-thick HDPE conversion layer for 14 MeV neutrons

E. Coincidence Test

To test the coincidence effect, the neutron spectrometer was used with the 14 MeV neutron beam stream at the China Institute of Atomic Energy Sciences (CIAES). The placement of the beam pipe and neutron spectrometer at the beam exit of CIAES is shown in Fig. 23 [FIGURE:23]. The neutron beam reached the experimental room through a metal pipeline, with minimal equipment in the experimental room. The beam spot diameter was small, resulting in lower gamma background. The neutron spectrometer was placed directly in front of the neutron beam pipe exit, and after irradiation, multichannel spectra from multiple detectors were recorded and analyzed.

Fig. 23. (Color online) Anti-coincidence test environment

In front of Detector No. 7, there was an HDPE conversion layer where neu-

trons reacted with hydrogen nuclei to produce recoil protons of 0 MeV to 14 MeV, which passed through the silicon detector to produce deposition energy. A corresponding simulation was performed using Geant4 following the same experimental configuration. Figure 24 [FIGURE:24] shows the relationship between the total deposition energy in detectors No. 7 and 8 and the deposition energy in detector No. 7 for each event.

Fig. 24. (Color online) Simulated data for recoil protons detected by the 14 MeV neutron incident neutron spectrometer

Geant4 was used to simulate a certain number of 14 MeV neutrons incident vertically from the front of detector No. 1 to the neutron spectrometer, where colors represent the number of events. Figure 25 [FIGURE:25] shows data measured under the same conditions. Two bands are evident in both plots when compared. The upper band with a decreasing trend represents recoil protons that only penetrate detector No. 7 and not detector No. 8. In this case, the horizontal coordinate is the total energy E of the recoil protons, and the vertical coordinate is the energy ΔE that the recoil proton loses in detector No. 7 after penetration. For protons with energies higher than 60 keV, the energy lost per unit length in Si decreases monotonically with increasing proton energy; hence, the energy lost by the recoil proton in detector No. 7 decreases with increasing total energy lost by the recoil proton in both detectors No. 7 and 8. The lower band with an upward trend represents recoil protons that have penetrated both detectors No. 7 and 8. In this case, the horizontal coordinate is the total energy ΔE lost by the recoil protons in detectors No. 7 and 8 after penetration, while the vertical coordinate is the energy ΔE lost by the recoil protons after penetrating detector No. 7, and ΔE increases with increasing ΔE in the case of both penetrations.

Due to differences between the energy-channel correspondences of the two detectors in actual measurements and the effect of detector energy resolution, the recoil proton bands in the two-dimensional plots of measured data are not as concentrated as those in simulated results; nevertheless, they are clear enough to show the relationship between the ΔE of the proton in the Si detector and the total energy E. The results also demonstrate that particles penetrating more than one detector simultaneously can be extracted from the neutron signal using the back-coincidence method. The experiment also showed that events of particles penetrating multiple detectors can be measured simultaneously, guaranteeing subsequent extraction of the neutron signal by the inverse conformal method.

Fig. 25. (Color online) Recoil proton test data detected by the 14 MeV neutron incident neutron spectrometer

V. SUMMARY

In this study, a prototype neutron spectrometer payload for an LEO neutron detection mission was designed and completed. Beginning with detector combi-

nations, two configurations of 15 silicon detectors were used, and the hardware, firmware, and software designs of the neutron spectrometer were completed. In this process, we performed thermal neutron principle and detection efficiency tests using the nuclear reaction method with a 27 μm-thick LiF thermal neutron conversion layer, and fast neutron principle and detection efficiency tests for neutrons up to 14 MeV using the nuclear recoil proton method with a 300 μm-thick HDPE fast neutron conversion layer. Corresponding simulation analyses of the experiments were performed, and the experimental data and simulation results showed good agreement and met design expectations. The intrinsic detection efficiency of the probes for 14 MeV fast neutrons was 1.05%. The neutron spectrometer is expected to detect atmospheric albedo neutrons and lightning neutrons in orbit, identify lightning neutrons and atmospheric albedo neutrons based on the spatial distribution of lightning occurrences, and obtain their relative contributions.

ACKNOWLEDGMENTS

The authors would like to thank the staff of the "Institutional Center for Shared Technologies and Facilities of INEST, HFIPS, CAS," "Division of Ionizing Radiation Metrology, National Institute of Metrology (NIM), China," CIAE, and CSNS Back-n white neutron facility for their support during measurements.

AUTHOR CONTRIBUTIONS

All authors contributed to the study conception and design. Material preparation, data collection, and analysis were performed by Xiao-Li Wang, Shu-Cheng Shi, Chen-Yao Ma, and Yi-Ming Ma. The first draft of the manuscript was written by Chen-Yao Han and Yi-Ming Ma, and all authors commented on previous versions of the manuscript. All authors read and approved the final manuscript.

DATA AVAILABILITY

All authors contributed to the study conception and design. Material preparation, data collection, and analysis were performed by Xiao-Li Wang, Shu-Cheng Shi, Chen-Yao Ma, and Yi-Ming Ma. The first draft of the manuscript was written by Chen-Yao Han and Yi-Ming Ma, and all authors commented on previous versions of the manuscript. All authors read and approved the final manuscript.

CONFLICT OF INTEREST

The authors declare that they have no competing interests.

REFERENCES

[1] B. Klecker, Energetic particle environment in near-Earth orbit. *Adv. Space Res.* 17, 37–45 (1996). doi:10.1016/0273-1177(95)00510-L

[2] P. Jiggens, C. Clavie, H. Evans et al., In situ data and effect correlation during September 2017 solar particle event. *Space Weather* 17, 99–117 (2019). doi:10.1029/2018SW001936
[3] S.F. Singer, Trapped albedo theory of the radiation belt. *Phys. Rev. Lett.* 1, 300 (1958). doi:10.1103/PhysRevLett.1.181
[4] M.I. Dobynde, Y.Y. Shprits, Radiation environment created with GCRs inside a spacecraft. *Life Sci. Space Res.* 24, 116–121 (2020). doi:10.1016/j.lssr.2019.09.001
[5] Z. Kopal, Physics of the Sun. *Br. J. Appl. Phys.* 7, 119 (1956). doi:10.1088/0508-3443/7/4/301
[6] L. Heilbronn, K. Frankel, K. Holabird et al., Production of neutrons from interactions of GCR-like particles. *Acta Astronaut.* 42, 363–373 (1998). doi:10.1016/S0094-5765(98)00131-3
[7] L.P. Babich, Generation of neutrons in giant upward atmospheric discharges. *Jetp Lett.* 84, 285–288 (2006). doi:10.1134/S0021364006180020
[8] W. Xu, S. Celestin, V.P. Pasko, Monte Carlo simulation of neutron generation by lightning leaders. *J. Geophys. Res. Space Physics* 120, 1355–1370 (2015). doi:10.1109/USNC-URSI-NRSM.2013.6525017
[9] R.S. Selesnick, M.D. Looper, R.A. Mewaldt, A theoretical model of the inner proton radiation belt. *Space Weather* 5, S04003 (2007). doi:10.1029/2006SW000275
[10] J.F. Valdés-Galicia, Y. Muraki, K. Watanabe et al., Solar neutron events as a tool to study particle acceleration at the Sun. *Adv. Space Res.* 43, 565–572 (2009). doi:10.1016/j.asr.2008.09.023
[11] H.Y. Huang, Z.Y. Zou, J.H. Hu et al., Characteristics of radiation belt energetic protons and the movement of their core location in response to geomagnetic disturbances. *Phys. Fluids* 36, 076601 (2024). doi:10.1063/5.0216361
[12] X.L. Li, R. Selesnick, Q. Schiller et al., Measurement of electrons from albedo neutron decay and neutron density in near-Earth space. *Nature* 552, 382–385 (2017). doi:10.1038/nature24642
[13] X.X. Yu, H. Lu, G.T. Chen et al., Detection of solar neutron events and their theoretical approach. *New Astron.* 39, 25–35 (2015). doi:10.1016/j.newast.2014.12.010
[14] K. Koga, Y. Muraki, S. Masuda et al., Measurement of solar neutrons on 05 March 2012, using a fiber-type neutron monitor onboard the attached payload to the ISS. *Sol. Phys.* 292, 115 (2017). doi:10.1007/s11207-017-1135-y
[15] T. Enoto, Y. Wada, Y. Furuta et al., Photonuclear reactions triggered by lightning discharge. *Nature* 551, 481–484 (2017). doi:10.1038/nature24630
[16] L.P. Babich, Radiocarbon production in thunderstorm storms. *Geophys. Res. Lett.* 44, 191–11,200 (2017). doi:10.1002/2017GL075131
[17] Q.Q. Shi, C.Y. Han, Q.G. Zong et al., Lightning-induced neutrons as a possible source of charged particles in the Earth' s inner radiation belt. *Earth Planet. Phys.* 9(2), 444–451 (2025). doi:10.26464/epp2025014
[18] J.E. Keith, G.D. Badhwar, D.J. Lindstrom, Neutron spectrum and dose-equivalent in shuttle flights during solar maximum. *Nucl. Tracks Radiat. Meas.* 20, 41–47 (1992). doi:10.1016/1359-0189(92)90083-8

[19] V.E. Dudkin, Y.V. Potapov, A.B. Akopova et al., Differential neutron energy spectra measured on spacecraft in low earth orbit. *Nucl. Tracks Radiat. Meas.* 17, 87–91 (1990). doi:10.1016/1359-0189(90)90188-4
[20] A.M. Preszler, S. Moon, R.S. White, Atmospheric neutrons. *J. Geophys. Res.* 81, 4715 (1976). doi:10.1029/JA081i025p04715
[21] V.I. Lyagushin, V.E. Dudkin, Y.V. Potapov et al., Russian measurements of neutron energy spectra on the Mir orbital station. *Radiat. Meas.* 33, 313–319 (2001). doi:10.1016/S1350-4487(00)00156-6
[22] H. Matsumoto, T. Goka, K. Koga et al., Real-time measurement of low-energy-range neutron spectra on board the space shuttle STS-89 (S/MM-8). *Radiat. Meas.* 33, 321–333 (2001). doi:10.1016/S1350-4487(00)00157-8
[23] G.H. Shen, S.Y. Zhang, X.G. Zhang et al., Using energy particle detection technology on the Tiangong' s Space Station' s Wentian Laboratory Cabin Module. *Aerospace* 10, 373 (2023). doi:10.3390/aerospace10040373
[24] G.H. Shen, D.H. Hou, Y. Chang et al., Neutron observations from the energetic particle detector on China' s Space Station. *Earth Planet. Phys.* 9(2), 460–466 (2025). doi:10.26464/epp2024078
[25] Z.L. Tang, M. Shen, Performance and evaluation for pixel CdZnTe detector of different thickness. *Adv. Mat.* 1015, 101 (2014). doi:10.4028/www.scientific.net/AMR.1015.101
[26] L.Y. Liu, X. Ouyang, R.L. Gao et al., Latest developments in room-temperature semiconductor neutron detectors: Prospects and challenges. *Sci. China Phys. Mech. Astron.* 66, 232001 (2023). doi:10.1007/s11433-022-2021-6
[27] W. Gao, S. Li, Y. Duan et al., Design and characterization of a low-noise front-end readout ASIC in 0.18-μm CMOS technology for CZT/Si-PIN detectors. *IEEE Trans. Nucl. Sci.* 65, 1203–1211 (2018). doi:10.1109/TNS.2018.2826070
[28] S. Zhao, C. Gao, X. Tian et al., A high counting-rate readout ASIC for CZT detectors. *Nucl. Instrum. Methods Phys. Res., Sect. A* 1064, 169416 (2024). doi:10.1016/j.nima.2024.169416
[29] R. He, X.Y. Niu, Y. Wang et al., Advances in nuclear detection and readout techniques. *Nucl. Sci. Tech.* 34, 205 (2023). doi:10.1007/s41365-023-01359-0
[30] X. Zhu, C.Q. Feng, Q. Li et al., FPGA-based real-time n/ discrimination with liquid scintillator. *IEEE Trans. Nucl. Sci.* 65, 2877–2882 (2018). doi:10.1109/TNS.2018.2877598
[31] Y.P. Cheng, W.L. Guo, Z.Y. Tang et al., Mission and payload design for in-situ detection of lunar regolith neutron radiation environment. *J. Space Sci. Exp.* 1, 63–71 (2024). doi:10.19963/j.cnki.2097-4302.2024.01.007
[32] C.J. Stapels, E.B. Johnson, X.J. Chen et al., Space neutron spectrometer design with SSPM-based instrumentation. *Nucl. Instrum. Methods Phys. Res. A* 652, 342–346 (2011). doi:10.1016/j.nima.2010.10.050
[33] Z.Y. Zhu, M.Q. Pu, M. Jiang et al., Bonding processing and 3D integration of high-performance silicon PIN detector for ΔE-E telescope. *Processes* 11, 627 (2023). doi:10.3390/pr11020627
[34] S.N. Wang, M. Yu, D.Y. Tian et al., Fabrication and characterization of thin silicon PIN detectors. *ECS Trans.* 60, 1165 (2014). doi:10.1149/06001.1165ecst
[35] C.Y. Han, S. Wang, Q.Q. Shi et al., A background suppression detector array for fast neutron measurement space science study. *Measurement* 230,

114479 (2024). doi:10.1016/j.measurement.2024.114479
[36] C.L. Zhou, S.F. Li, C.X. Xu, Study on influence factors of the peak-to-Compton ratio of the HPGe -ray spectrometer system based on the anti-coincidence measuring technique. *Nucl. Electron. Detect. Technol.* 26, 429–433 (2006). doi:10.3969/j.issn.0258-0934.2006.04.011
[37] H.M. Gerstenberg, R.S. Caswell, J.J. Coyne, Neutron-induced secondary charged particle spectra. *Radiat. Prot. Dosim.* 23, 43 (1988). doi:10.1093/oxfordjournals.rpd.a080126
[38] J.Y. Yang, L. Li, H.W. Lyu et al., A calculation method for parameters of secondary neutron source in nuclear reactor. *Nucl. Tech.* 41, 060605 (2018). doi:10.11889/j.0253-3219.2018.hjs.41.060605
[39] G.H. Zhang, J.M. Liu, Z.H. Xue et al., Measurement of ^{1}B content in thin-film ^{1}B samples. *Appl. Radiat. Isot.* 69, 858–861 (2011). doi:10.1016/j.apradiso.2011.02.017
[40] A. Omar, S. Burdin, G. Casse et al., GAMBE: Thermal neutron detection system based on a sandwich configuration of silicon semiconductor detector coupled with neutron reactive material. *Radiat. Meas.* 122, 121–125 (2019). doi:10.1016/j.radmeas.2019.01.019
[41] J.S. Wan, G.N. Zhu, Y. Zhao et al., Computer studies of detection efficiency of fast-neutron spectrum based on PADC using the Monte Carlo method. *Radiat. Meas.* 36, 193–197 (2003). doi:10.1016/S1350-4487(03)00122-7
[42] Y.M. Ma, Research and design of space neutron detection system. Weihai, China: Shandong University. 2023. doi:10.27272/d.cnki.gshdu.2023.006159
[43] C.Y. Han, Simulation and test of neutron spectrometer in near-Earth orbit. Weihai, China: Shandong University. 2022. doi:10.27272/d.cnki.gshdu.2022.003927
[44] T.Z. Chen, X.H. Li, K. Wang et al., A readout electronic system for a 3D position-sensitive CdZnTe gamma-ray spectrometer based on the CPRE10-32 readout ASIC. *J. Instrum.* 17, T10005 (2022). doi:10.1088/1748-0221/17/10/T10005
[45] S.Y. Ma, S.B. Liu, H. Liu et al., A SKIROC2-based prototype electronics system for silicon PIN array. *Radiat. Detect. Technol. Methods* 2, 36 (2018). doi:10.1007/s41605-018-0060-4
[46] Y.X. Liu, S. Zhang, Y.K. Qian et al., Monte Carlo simulation study on the ^{2} ^{1}Am-Be radionuclide source reference neutron radiation. *Nucl. Technol. Radiat. Prot.* 35, 283–293 (2020). doi:10.2298/NTRP2004283L
[47] W.H. Zhang, H.B. Kang, Y.J. Wang et al., Development of a portable single sphere neutron spectrometer. *Radiat. Meas.* 140, 106509 (2021). doi:10.1016/j.radmeas.2020.106509
[48] P.Q. Wang, J.K. Yang, F. Li et al., Thermal neutron reference radiation facility with high thermalization and large uniformity area. *Metrologia* 60, 45002 (2023). doi:10.1088/1681-7575/acd6fb
[49] R. García-Baonza, G.F. García-Fernández, E. Gallego et al., A novel conceptualization in the analysis and design of passive neutron area monitors based on gold foil activation. *Appl. Radiat. Isot.* 181, 110110 (2022). doi:10.1016/j.apradiso.2022.110110
[50] R. Tursinah, S. Permana, Z. Su' ud et al., Design and validation of a single

cylindrical neutron spectrometer using a gold activation foil. *Radiat. Meas.* 171, 107053 (2024). doi:10.1016/j.radmeas.2024.107053
[51] W. Jiang, H.Y. Jiang, H. Yi et al., Detector calibration based on secondary protons at the Back-n white neutron source. *Acta Phys. Sin.* 70, 082901 (2021). doi:10.7498/aps.70.20201823